Available online at www.sciencedirect.com

ScienceDirect

Journal of Magnesium and Alloys 8 (2020) 472–479

www.elsevier.com/locate/jma

Full Length Article

Strong strain path dependence of strain localizations and fracture in magnesium AZ31 sheet

Kıvanç Alkan, O. Berk Aytuna, Baran Güler, Mert Efe*

Department of Metallurgical and Materials Engineering, Middle East Technical University, Ankara 06800, Turkey

Received 25 September 2019; received in revised form 9 March 2020; accepted 15 March 2020
Available online 18 May 2020

Abstract

This study compares the deformation and fracture behavior of a basal-textured Mg AZ31 alloy sheet under uniaxial tension and biaxial stretching by using an in-plane biaxial test setup capable of observing and measuring the deformation at both meso (millimeter) and microstructure scales. Strain distributions at the mesoscale and accompanying fracture surfaces indicate a significant dependence on strain path. At the microscale, limited slip activity in biaxial case promotes contraction twins, where severe strain localizations ($\varepsilon_{max}/\varepsilon_{mean} \approx 20$) to the twins and their boundaries cause mainly transgranular fracture. This leads to a brittle, and a more pronounced shear-type fracture under biaxial stretching. In uniaxial case, considerable tensile twinning activity reorients the initial texture for slip activity. Strain localizations ($\varepsilon_{max}/\varepsilon_{mean} \approx 2$) to the grain interiors and boundaries initiate mainly intergranular fracture. Samples fail by displaying both brittle and ductile fracture structures, with smaller shear lips compared to the biaxial case.

Keywords: Formability; Twinning; Biaxial; DIC; AZ31.

1. Introduction

Formability of magnesium alloys is highly sensitive to the loading conditions. In AZ31 magnesium alloys with a strong basal texture and small grain size ($d < 10$ μm), equivalent fracture strains can be 5 times higher under uniaxial tension compared to biaxial stretching [1]. The basal slip has zero Schmid factor for the original basal-textured grains under uniaxial tension, however it may be activated once the twins rotate the grains into favorable orientations [2,3]. Prismatic slip also contributes to the enhanced formability in the uniaxial case [4,5]. Despite the strains are uniformly distributed at the macroscale [4,6], recent microstructure scale investigations reveal that there is a significant inhomogeneity in deformation of magnesium alloys under uniaxial loading [7–10]. Even when the prismatic slip is active, the number of active slip systems do not satisfy the Taylor Criteria. Strain localizes at the favorably oriented grains, grain boundaries [8], {10-11} contraction and {10-11}-{10-12} double twins [11], creating a non-homogeneous deformation. While the exact sources of fracture are unclear, post-fracture studies indicate double twins as the primary candidate [11–13]. Recent in-situ electron microscopy studies show crack propagation along both {10-12} tension and contraction twins [14].

Lack of microscale studies for biaxial stretching limits the identification of deformation mechanisms and prevents the correlation of microstructural features to the poor formability. As the equal transverse and longitudinal loads cancel each other during biaxial stretching, the prismatic slip becomes inactive [15]. Contraction twins and some limited basal slip become the only possible deformation mechanisms, yet some studies showed that the contribution of twinning is minimal [15–17]. Contraction twinning may have a critical role in biaxial stretching and enhance the formability by reorienting the initial basal texture [1]. Despite being unfavorable under either biaxial or uniaxial loading, {10-12} tension twins have also been observed [1]. In addition to the ambiguity in the

* Corresponding author.
E-mail address: mefe@metu.edu.tr (M. Efe).

https://doi.org/10.1016/j.jma.2020.03.002

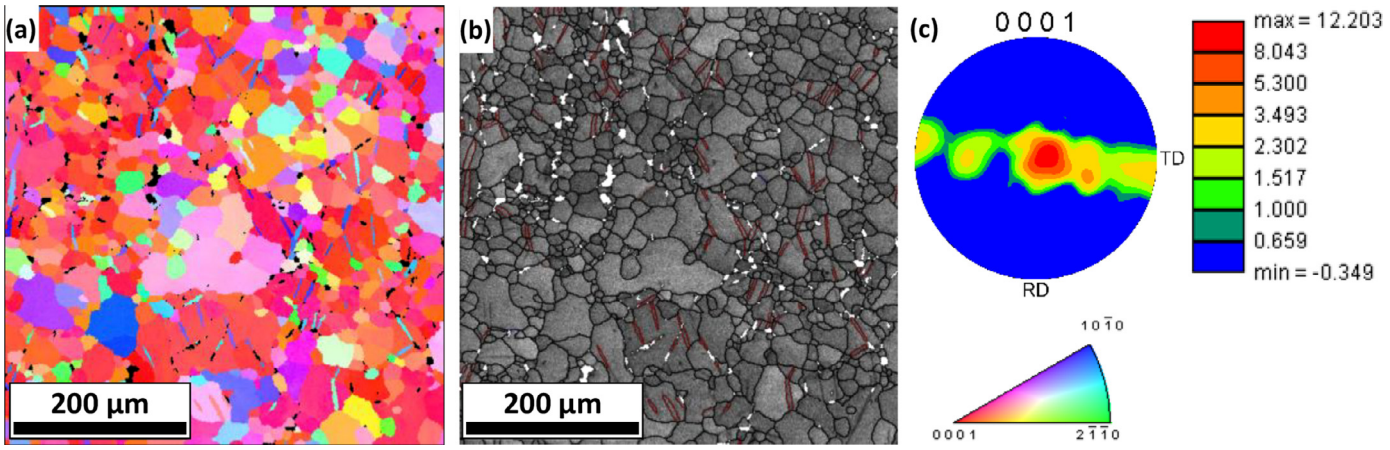

Fig. 1. EBSD results of the as-received sheet: (a) orientation distribution map of the TD-RD plane, (b) grain boundary misorientation map, where black lines are grain boundaries: >15°, red lines are tensile twin boundaries: 86.4 ± 5° around <-12-10> (c) (0001) pole figure of TD-RD plane.

active deformation mechanisms and their contribution, the microstructural origins of the strain localizations and the fracture under biaxial loading are also unclear. As the biaxial stress-state is dominant in most of the forming operations [16,17], a systematic study is needed to understand the twinning behavior, and its relation with the strain localizations and the ultimate failure of the material.

In this study, deformation and fracture mechanisms of a strongly basal-textured AZ31 magnesium alloy sheet are studied under uniaxial tension and biaxial stretching by a novel in-plane biaxial testing setup, which can achieve large strains and multi-axial strain paths. The setup is also capable of in-situ strain analyses in order to reveal the microstructural features and deformation mechanisms responsible from the forming behavior of the AZ31 alloy. For this purpose, the sheet with typical basal texture was tested until fracture, where the loading was parallel to the plane of the sheet.

2. Materials and methods

The microstructures and microtextures of the sheets before and after slight plastic deformation (2–3%) were characterized by the electron backscatter diffraction (EBSD) method. Samples were electropolished with a 800 ml ethanol, 18.5 ml distilled water, 75 g citric acid, 15 ml perchloric acid solution at −30 °C and 30 V for 450 s. The diffraction data was obtained by a FEI Quanta 200 FX scanning electron microscope equipped with EDAX EBSD camera. OIM software by EDAX was used for plotting the orientation maps, misorientation angle maps, and pole figures. Only data points with high correlation index were presented (CI > 0.05), where the black regions in the misorientation maps correspond to the omitted data points with low correlation index. The same microscope was also used to image the fracture surfaces of the samples. In this case, the electropolished samples were further chemically etched to reveal all the microstructural features.

The as-received, 2 mm-thick AZ31 sheets had a slightly shifted, strong basal texture, with an initial grain size of 40 ± 15 µm (Fig. 1(a)). There are also some large grains with off-basal texture (Fig. 1(a)). This kind of texture and microstructure are typical for rolled and annealed AZ31 sheets [4]. Some {10-12} tensile twins are also present in the microstructure with 86±5° misorientation angle (Fig. 1(b)). Pole figure (0001) from the TD-RD surface shows some spread due to the presence of tensile twins and off-basal grains, however the main texture is still concentrated around {0001} orientations (Fig. 1(c)).

Cruciform shaped samples for testing (Fig. 2(a)) were cut from the as-received sheets by water-jet. Then, a reduced cross-section was milled into the sample with a HAAS VF-1 computer numerical control (CNC) vertical milling machine to collect the stresses and strains at the center (Fig. 2(b)). The overall sample geometry and the dimensions are provided in Fig. 2(a) and (b). For testing, samples were attached to the compact and portable test apparatus (Fig. 2(c)), which was integrated to a Shimadzu Bending Test Machine with a capacity of 10 kN. The apparatus converts the vertical load from the test machine into the horizontal loads on the four arms of the sample (Video 1). In biaxial stretching configuration, sample was connected to the arms with equal length (equibiaxial loading) and the forces were monitored throughout the test with load cells attached to the each arm (Fig. 2(c)). In uniaxial loading, sample was attached only to the two arms by aligning rolling direction of the sheets parallel to the tensile direction. In both conditions, load difference between the arms did not exceed 100 N during the tests. For repeatability of the results, at least three samples were tested for each condition and the results reported here are the representation of the general behavior observed during the tests.

The in-situ strain measurements were done by the imaging unit (Fig. 2(d)), which has interchangeable optics that allow recording of images both at the millimeter (mesoscale) and the micrometer scale. Few hundred images were recorded during the tests and later analyzed by a 2D digital image correlation (DIC) software named Ncorr [18]. Incremental DIC was conducted and the image pairs were selected to satisfy a low correlation coefficient, without adding new features between two images. Field of view was 300×400 µm^2 at the mi-

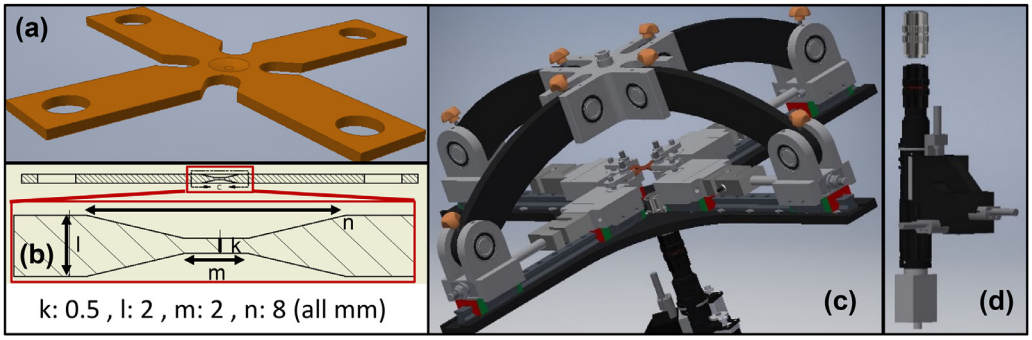

Fig. 2. Test setup: (a) 3D CAD model of the cruciform-shaped sample, (b) technical drawing and dimension table for the sample and its reduced cross-section, (c) test apparatus, (d) optical imaging unit.

croscale and it was the entire area of the reduced cross-section (3 mm^2) at the mesoscale (Fig. 2(b)). The imaging area was sprayed with a paint solution containing 30% of acrylic paint and 70% of acetone that resulted in randomly distributed ~ 20 μm size black dots (speckles) necessary for the correlation. For the microscale, the sample surfaces were electroetched with a 20% Nital solution at −30 °C and 12 V for 30 s. The grain boundaries and other features provided the contrast for correlation. As the interior of grains remained mostly featureless after etching, TiO_2 nanoparticles were sprayed to the sample surface, resulting in additional contrast by appearing as 1–5 μm sized dark particles. After the DIC, the strain maps were plotted in terms of Euler–Almansi strains. The strain values reported in the text were then converted to the true logarithmic strains by: $\varepsilon_{tr} = \ln(\sqrt{1/(-2\varepsilon_{EA}+1)})$. The reported average strain values were median rather than the mean, to eliminate the inevitable extreme strain values calculated by the DIC software. These extremes in both maxima and minima were a result of incorrect correlation and could affect the mean values. When the median is considered, these values cancel out each other and the median value becomes independent of the extremes. The maximum strain error calculated by rigid body translation was 0.18% and 0.14% at the microscale and mesoscale, respectively. The spatial strain resolution is 1.1 μm for microscale and 7.2 μm for mesoscale, as defined by the distance between data points located in a subset. In this case, the resolution is not limited by the imaging system capabilities, but rather by the size of the speckles and the subset. Details of the imaging unit, DIC parameters and speckle pattern preparation can be found in our previous publication [19].

3. Results and discussion

Distribution of major strains at the mesoscale shows heterogeneous deformation under both uniaxial tension (Fig. 3 top row) and biaxial stretching (Fig. 3 bottom row). Fig. 3(a) and (b) are the major strain maps for uniaxial tension and biaxial stretching at the onset of strain localizations. Inside the localizations, the equivalent true strains (ETS) doubles the median ETS. The median ETS are 0.038 for uniaxial tension and 0.016 for biaxial stretching at the onset of localizations, indicating that the localizations start slightly earlier in biaxial stretching. There are also more localized spots in this condition (Fig. 3(b)). These spots continue to accumulate strain until the sudden sample failure under biaxial stretching (Fig. 3(d)). In uniaxial tension case, the strain localizes into a local neck perpendicular to the major stain direction (Fig. 3(c)), and the sample fractures through the local neck. Here, the fracture is defined as the first observation of a through-thickness crack in the sample. While the median major and minor fracture true strains are different ($\varepsilon_{1,\ uniaxial} = 0.14$, $\varepsilon_{2,\ uniaxial} = -0.07$; $\varepsilon_{1,\ biaxial} = 0.07$, $\varepsilon_{2,\ biaxial} = 0.07$), the median equivalent true strains (ETS) for both uniaxial tension, ETS = 0.14 ± 0.05, and biaxial stretching, ETS = 0.14 ± 0.02, are comparable to each other (Fig. 3(e)). This is parallel to the results obtained in the literature for the relatively large grained AZ31 sheets (d ~ 40 μm, ETS = 0.17) [1]. The difference in ETS becomes significant as the grain size approaches to 5 μm [1]. In theory, the fracture ETS should change, as the stress triaxiality is expected to be different in each condition. The equivalent fracture strain in tension should be two times higher than biaxial, yielding a constant thickness strain and a constant slope of −1 in the $\varepsilon_1\varepsilon_2$ space [20]. Thus, the constant fracture ETS indicate a change in fracture mechanisms. The strain distribution in biaxial before fracture resembles an S shape (Fig. 3(d)), and the samples fail following the same pattern with sharp fracture surfaces. This behavior is similar to the shear controlled fracture of brittle solids.

In-situ observations at the microscale during uniaxial tension show the sources of strain localizations and fracture (Video 2, note that the video is faster than normal). Sample begins the deformation in the as-polished-etched, flat state. Contrast difference and orange peel like surface roughness form in some grains during the deformation due the surface undulations and protuberances. These grains accumulate major and minor strains and expand, indicating slip activity within the grains (Video 2). With further deformation, strain localizes to the grain boundaries. Simultaneously, slip-assisted grain boundary sliding at room temperature can be observed as described by Koike et al. [21]. Towards the end of the test, sharp narrow lines suddenly appear in multiple grains simultaneously. Video stills captured at the beginning, mid-point, and end of the test (before fracture) show the three distinct local-

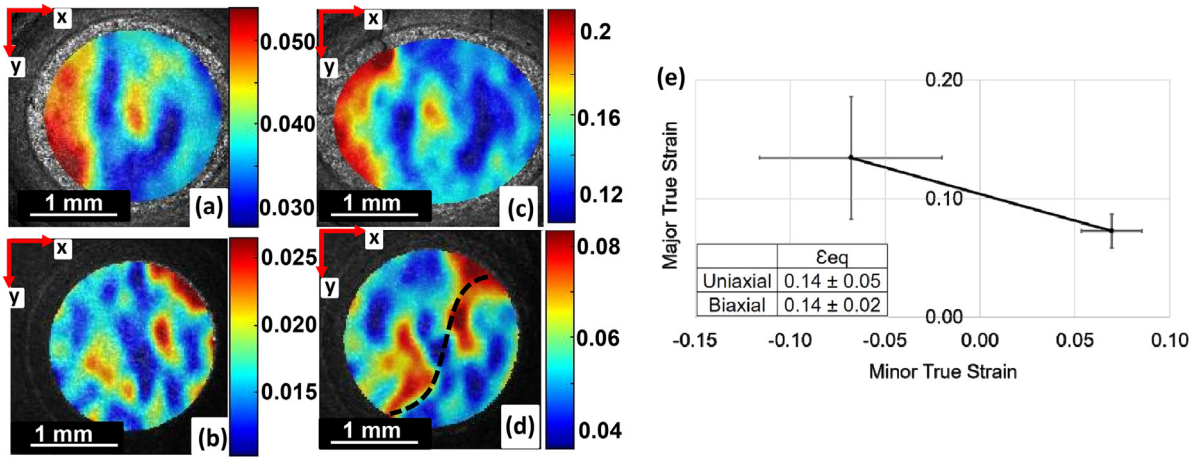

Fig. 3. Mesoscale major strain (ε_1) maps of deformed samples: (a) uniaxial tension at localization start, (b) biaxial stretching at localization start, (c) uniaxial tension before fracture, (d) biaxial stretching before fracture.

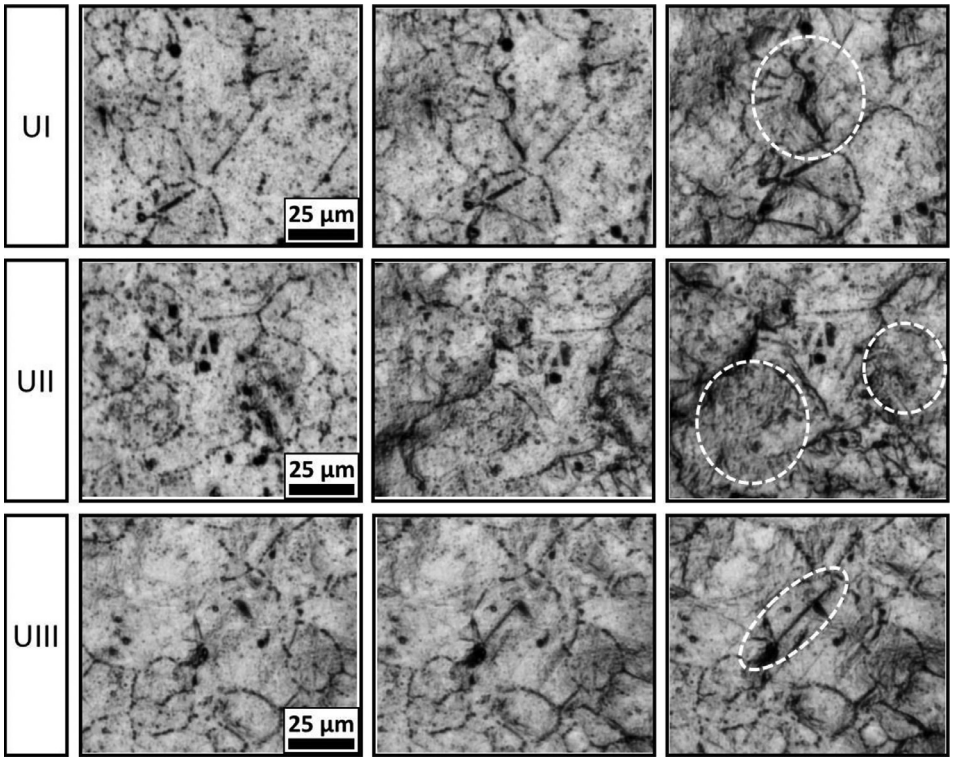

Fig. 4. Video stills captured during the uniaxial test: microscale images show three distinct localization mechanisms (indicated by white circles) in different regions of the sample.

ization mechanisms in the sample (Fig. 4). In region UI, slip concentration at the grain boundaries is visible by bulging-out of the boundaries in the thickness direction. Two neighboring boundaries form a ledge-like surface feature and microcracking accompanies this behavior (white circle in UI). In region UII, the mechanism is slip in the grains, which roughen and expand due to the slip activity. Orange peel like roughness and surface protuberances are the distinct features of the slip activity inside the grains (white circles in UII). In region UIII, slip is limited in the middle grain, which rather develops a sharp, narrow band in it. Thickening and darkening of the band are indications of strain concentration within the band, which has similar appearance to the twins developing in Mg alloys. The small grains in the bottom right corner of this region show slip activity similar to grains in UII.

Strain maps obtained at a median ETS = 0.11 quantifies the strain localization in slipped (UI and UII) and banded regions (UIII) of the sample (Fig. 5). Deformation is heterogeneous and the maximum ETS of the slipped regions (UI and UII) are about 2 times higher than the median ETS (Table 1). Compared to the banded areas (UIII), slip at the grain boundaries (UI) and in the grains (UII), yield higher

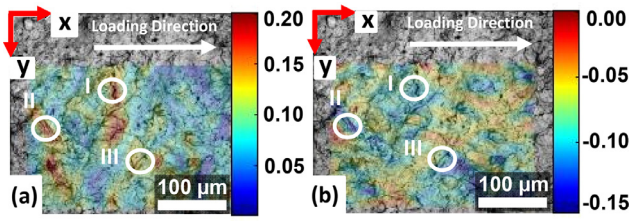

Fig. 5. Microscale strain maps of the uniaxial sample: (a) major strain, ε_1 (b) minor strain, ε_2.

Table 1
Strain values of the localized regions and the median strains of the maps.

Regions	$\mathcal{E}_1$	$\mathcal{E}_2$	$\mathcal{E}_{eq}$	$\mathcal{E}_{1,median}$	$\mathcal{E}_{2,median}$	$\mathcal{E}_{eq,median}$
UI	0.21	−0.10	0.21			
UII	0.21	−0.13	0.21	0.10	−0.09	0.11
UIII	0.13	−0.10	0.14			
BI	0.29	0.07	0.38	0.016	0.001	0.02
BII	0.16	0.04	0.21			
BIII	0.04	0.03	0.07	0.034	0.002	0.04

average major and minor strain values, whereas the ratio of major to minor strains is in agreement with the uniaxial strain path (Table 1). Moreover, localizations to the narrow bans (presumably twins) account only 1.4% of the global strain, whereas localizations due to the slip constitute the major part of the deformation (29.3%).

In-situ recordings during the biaxial stretching tests show negligible deformation within the grains, instead narrow bands form suddenly and simultaneously along random grains (Video 3, note that the video is faster than normal). As the amount of deformation increases, strain further localizes to the narrow lines, which get thicker and reach to the grain boundaries (Video 3). Here, the in-situ recordings do not provide enough evidence as the narrow lines being twin boundaries. Indeed twin boundaries can only become visible after etching. In this case, the lines can be the result of strain accumulating at the twin boundaries or within the twins. Video stills captured during the tests show the two distinct localization mechanisms for the biaxial stretching (Fig. 6). Region BI is where the strain localizes to the bands. These dark black lines are the potential markers of the twinned areas, and similar to the uniaxial case they slowly grow during the test. Region BII is another localized spot, where the main source of strain concentration is the microcracks forming at the grain boundaries. In this case, however, the neighboring grains do not show any considerable slip activity. Microscale investigations from another sample, on the other hand, indicate some slipping activity within the grains, which bulge and deform as a result of the slip activity (Region BIII, video is not provided).

Microscale strain maps at a median ETS = 0.02 quantify the intensity of the localizations in regions BI and BII (Fig. 7). Their strains are considerably higher and anisotropic compared to the other regions in the sample (Fig. 7 and Table 1). Major strains are almost 4 times higher than the minor, consistent with the orientation of the bands with respect to the loading direction. The bands almost exclusively align perpendicular to the major strain direction and limit any deformation along the minor strain direction. In both BI and BII, and other banded regions, the ETS are nearly 20 times greater than the median ETS (Table 1). The contribution of these regions to overall deformation is 26.4%, with almost no contribution from the slipped regions. Within the slipped regions (BIII, strain map not provided), the major and minor strains are nearly equal (0.04 and 0.03), as expected from the biaxial stretching. In this case, the equivalent strain of BIII is 0.07, which is close to the median ETS of the sample (Table 1). Since the strain accumulation in this region is not as severe compared to the banded regions, slipped regions are not considered as localized spots for the biaxial tests. The limited amount of slip activity causes an imbalance in the median major and minor strains during the biaxial tests, where the major is almost 10 times higher than the minor (Table 1). This imbalance may be responsible from the unusual fracture behavior observed at the macroscale. It also confirms that the anisotropic strain accumulation in the banded regions undertake majority of the overall deformation.

In order to identify the microstructural features responsible from the localizations, deformed samples were characterized by EBSD. The EBSD data was not collected from the same location of the strain maps and the quality of the data

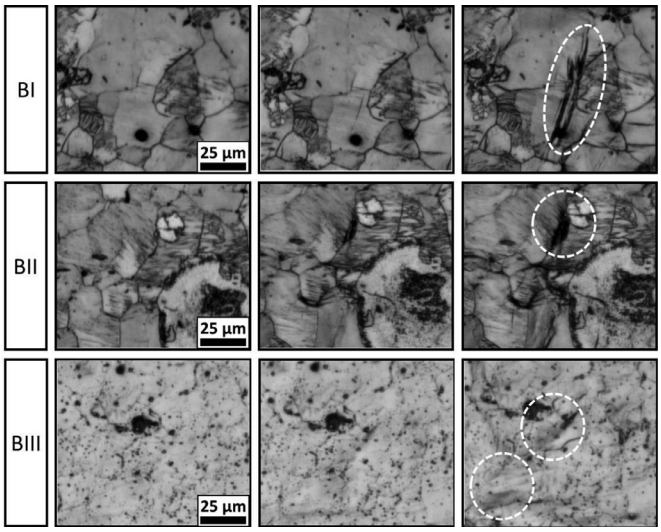

Fig. 6. Video stills captured during the biaxial test: Microscale images show two distinct localization mechanisms, BI and BII, (indicated by white circles) in different regions of the sample. Region BIII is from another sample and do not show severe localization.

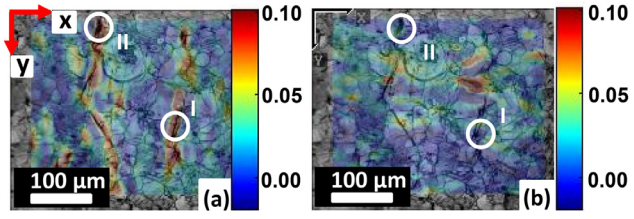

Fig. 7. Microscale strain maps of the biaxial sample: (a) major strain, ε_1 (b) minor strain, ε_2.

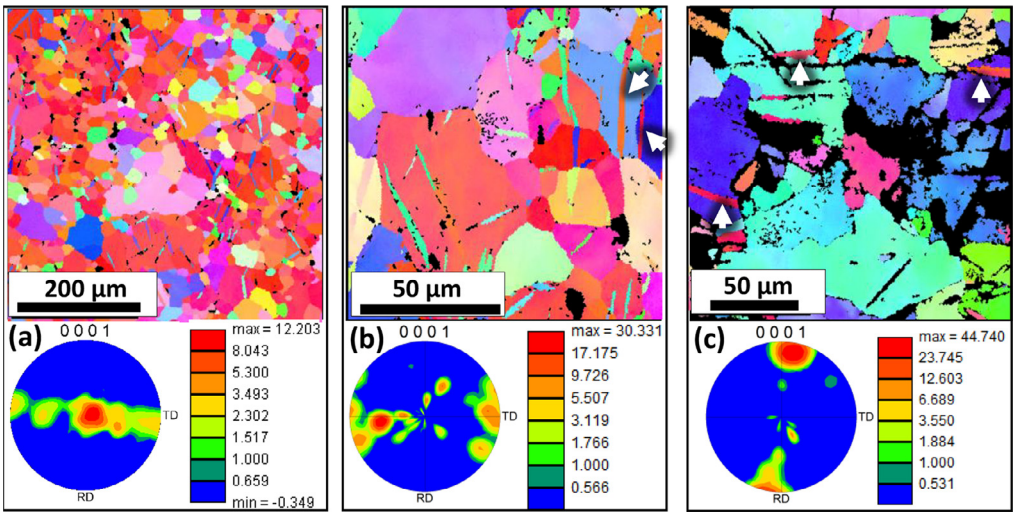

Fig. 8. Orientation distribution maps of the TD-RD plane and associated (0001) pole figures of the Mg sheets: (a) as-received, (b) biaxial stretching, $\varepsilon_{eq} = 0.029$, (c) uniaxial tension, $\varepsilon_{eq} = 0.025$.

was not perfect due to the deformation, yet it was enough to pinpoint the microstructural sources of the observed deformation behavior. Compared to the as –received state (Fig. 8(a)), the amount of tension twins slightly increases with biaxial stretching (Fig. 8(b)). The type of twins was confirmed by the misorientation angle of 86.4° around <-12-10>. The initial texture slightly shifts as some grains appear to be rotated due to either twins or slip (Fig. 8(b)). With uniaxial tension, there is almost a complete reorientation of the initial texture by almost 90° (Fig. 8(c)). There are again some indications of tension twins (Fig. 8(c) – white arrows), but indeed they are residues of the initial texture. Tension twins re-orient the initial texture and consume the entire grains as they grow, leaving the remnants of initial basal-textured grains appearing as twins. During the rotation of texture, C-axis remains perpendicular to the RD and instead aligns with the TD. It is also possible to find similar grains in the biaxial sample, where the tension twins consume almost all of the initial grains (Fig. 8(b) – white arrows). Although tension twin formation is unlikely under both uniaxial tension and biaxial stretching [22], there are some examples for this unexpected behavior in literature [1,10,23–25]. Slightly shifted basal texture and the tension twins in the initial microstructure may have caused the easy growth of {10-12} twins. Complicated internal stresses [1] and crack initiation [24] may be the other factors to initiate the twins. Anisotropic and heterogeneous of deformation may have switched the local stresses from tension to compression.

Independent of the exact sources of tension twins, their activity is clear under uniaxial loading. Otherwise, a complete reorientation of the texture would not be possible with slip only. Then, the most likely candidate for the strain localized bands towards the end of uniaxial test (Fig. 4 – UIII), is the remaining basal textured regions that is left-over from the tension twins (Fig. 8(c)). The texture difference between these regions and the re-oriented regions may have caused the strain localizations. However, strain localizations to these regions are minor as the majority of the deformation happens within the grains and along the grain boundaries, which explains to the loss of diffractions data in some grains and boundaries (Fig. 8(c)). Indeed, the complete reorientation of texture may actually be beneficial in delaying strain localizations at the early stages of the deformation [10].

In addition to the presence of {10-12} twins, contraction and double twins should be dominant in the tests. They are harder to observe with EBSD, but optical images provide evidence for their existence, especially under biaxial stretching (Fig. 6). Their appearance and behavior are identical to what has been observed in the literature [26], being narrow and not expanding with further strain. Detailed TEM studies from these twins indicate they are actually {10-11}-{10-12} type double twins [26]. Then, the most likely sources of the severe strain localized regions in biaxial are the contraction or double twins. These twins reorient the texture for basal slip to be favorable in them. The strain concentration into the twins or their boundaries may have formed the dark bands appearing towards the end of the test (Fig. 6 – BI). In tension, on the other hand, there is lack of evidence for either contraction or double twins. Slip activity after the re-orientation of texture may have suppressed these twins.

Misorientation data provides evidence for slip activity in both biaxial and uniaxial tension (Fig. 9(b) and (c)). However, in uniaxial, there is more grain fragmentation and corresponding low-angle subgrains. Two peaks at the beginning (0°–5°) and at the end (85°–90°) of the misorientation distribution correspond to the subgrains in the initial and reoriented grains, respectively (Fig. 9(c)). As the basal slip activity would be limited in the reoriented grains, prismatic slip becomes the main contributor to the deformation [27]. Indeed, *C*-axis being perpendicular to the tensile loading direction is shown to promote the prismatic slip [27]. The prismatic slip may lower the intensity of strain localizations at the grain

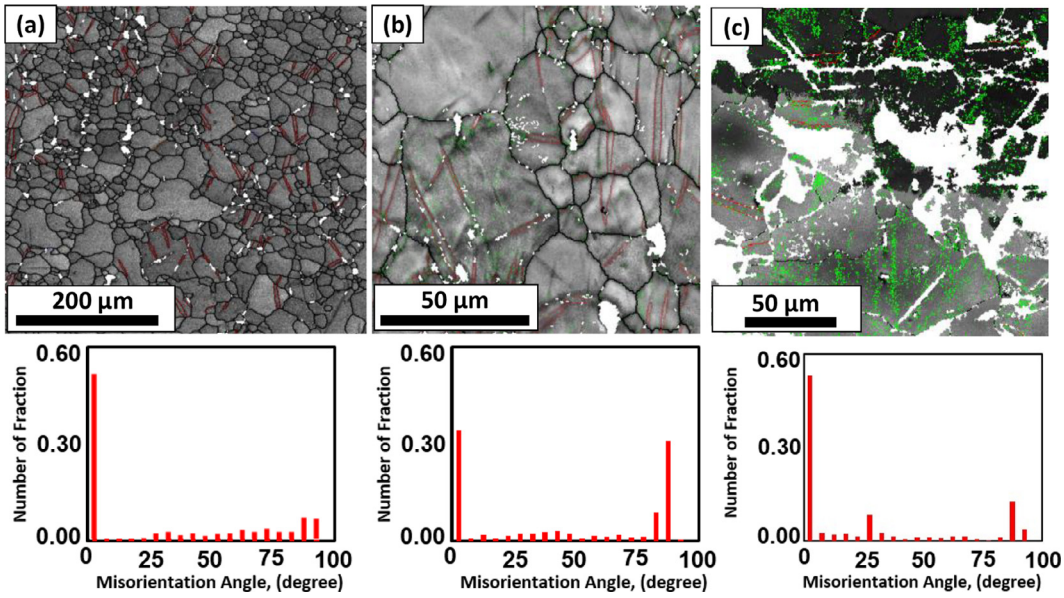

Fig. 9. Boundary misorientation maps and distributions of the Mg sheets: (a) as-received, (b) biaxial stretching (c) uniaxial tension. Black (>15°) and green (<5°) are grain boundaries. Red lines are tensile twin boundaries: 86.4 ± 5° around <-12-10>. Misorientation <3° are omitted.

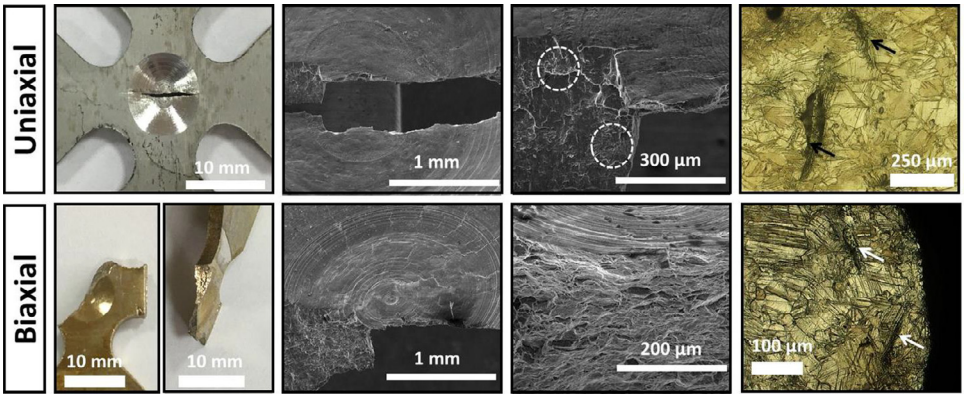

Fig. 10. Photos, SEM pictures, and optical microstructures of the failed samples: (top row) uniaxial, (bottom row) biaxial.

boundaries ($\varepsilon_{max}/\varepsilon_{mean} \approx 2$) when compared to the previous microscale studies where the basal slip dominated the deformation ($\varepsilon_{max}/\varepsilon_{mean} \approx 30$) [8]. The results in this study are rather comparable to the previous microscale studies on the randomly textured Mg alloys ($2 < \varepsilon_{max}/\varepsilon_{mean} < 5$), where prismatic and basal slip are both active [7,9]. The complete shutdown of prismatic slip in biaxial results in lower amount of subgrains (Fig. 9(b)), but there appears to be some basal slip within the initial grains having tilted basal orientations. Combined with the twinning activity, the basal slip shifts the initial texture towards TD.

As with the strain localization behavior, fracture of samples is quite different under uniaxial and biaxial strain paths (Fig. 10). While the sample fails by a single, straight crack perpendicular to the loading direction in uniaxial, the crack has an S shape in biaxial and it is slanted. The crack path follows the S-shaped strain distribution at the mesoscale, with a larger shear lip compared to the crack in uniaxial. Fracture surfaces in uniaxial contain indications of ductile fracture both in the shear lip and in the crack body (Fig. 10 – white circles), whereas ductile fracture features are absent in biaxial. Chemical etching of the fractured surfaces reveals the sources of fracture initiation (Fig. 10 – optical images). Uniaxial sample contains small amount of twins and strain-localized areas, due to the dominance of the slip over twinning. Cracking along grain boundaries is evident (Fig. 10 – black arrows), parallel to the in-situ observations (Fig. 4). The sample eventually fails by microcracks propagating along the grain boundaries. A significant number of twins are present in the fractured biaxial sample. Severe strain localization to the twins leads to microcracking along them (Fig. 10 – white arrows). These microcracks then reach to the grain boundaries, where they are linked with each other (Fig. 6). A mixture of transgranular and intergranular fracture occurs at the ultimate sample failure. Some independent microcracks form at the grain boundaries, however, microcracks originating from the twins prevail and control the overall fracture, which is brittle and shear-type.

4. Summary

In this study, strain localizations in basal-textured magnesium are investigated under uniaxial tension and biaxial stretching. The samples are tested until fracture, which enabled characterization of the effects of strain localizations on the fracture. Detailed analyses of the in-situ recordings, strain maps and microstructure lead to the following observations:

- The fracture strains are similar (ETS $\approx$ 0.14) under both uniaxial tension and biaxial stretching. This indicates a change in fracture mechanism with strain path, as in theory the fracture strains in tension should be two times higher than biaxial for a given material with constant fracture behavior. The strain distributions before fracture are also markedly different, where strains are concentrated along a straight band under uniaxial and an S-shaped band under biaxial. The samples then fracture along the same patterns.
- The primary candidates for strain localizations are contraction or double twins and their boundaries in biaxial, where the localized ETS are 20 times greater than average ETS values. The major strain is significantly higher than the minor, both in strain localized regions and in the gage area, confirming twinning-dominated deformation. 26% of the global strain accumulates in the twinned regions, where slip is limited throughout the sample. Within the slipped regions, the major and minor strains are almost equal.
- Considerable {10-12} tension twinning in uniaxial reorients the initial texture, and allow some slip activity. Slip causes deformation within the grains and the grain boundaries. The intensity of strain localizations is lower, where localized ETS are 2 times higher than the average. The major strains are also 2 times higher than the minor in both the localized regions and the gage area, as expected from the uniaxial strain path. Almost 30% of the global strain accumulates in the localized regions. Other regions of the sample also deform by slip, where the accumulated strains are close to the average.
- Microcracks initiate at the strain localized regions under both strain paths. In biaxial, microcracks grow along the twins and the grain boundaries, leading to a mainly transgranular fracture. At the eventual sample failure, the slanted crack lacks ductile fracture features and contains a large shear lip. Microcracks initiate at the grain boundaries in uniaxial due to the increased slip activity. Fracture is mainly intergranular, and the failed sample display features of both ductile and brittle fracture. The shear lip is much smaller compared to the biaxial.

Acknowledgments

This work was supported by European Commission's Research Executive Agency's Marie Skłodowska-Curie Actions – Career Integration Grant (FP7-PEOPLE-2013-CIG) with grant agreement #631774.

Supplementary materials

Supplementary material associated with this article can be found, in the online version, at doi:10.1016/j.jma.2020.03.002.

References

[1] Y. Chino, K. Kimura, M. Mabuchi, Acta Mater. 57 (2009) 1476–1485, doi:10.1016/j.actamat.2008.11.033.
[2] M.R. Barnett, M.D. Nave, C.J. Bettles, Mater. Sci. Eng. A 386 (2004) 205–211, doi:10.1016/j.msea.2004.07.030.
[3] L. Jiang, J.J. Jonas, A.A. Luo, A.K. Sachdev, S. Godet, Scr. Mater. 54 (2006) 771–775, doi:10.1016/j.scriptamat.2005.11.029.
[4] K. Yoshida, Int. J. Plast. 84 (2015) 102–137, doi:10.1016/j.ijplas.2016.05.004.
[5] J. Koike, T. Kobayashi, T. Mukai, H. Watanabe, M. Suzuki, K. Maruyama, K. Higashi, Acta Mater. 51 (2003) 2055–2065, doi:10.1016/S1359-6454(03)00005-3.
[6] M. Marya, L.G. Hector, R. Verma, W. Tong, Mater. Sci. Eng. A 418 (2006) 341–356, doi:10.1016/j.msea.2005.12.003.
[7] G. Martin, C.W. Sinclair, J.H. Schmitt, Scr. Mater. 68 (2013) 695–698, doi:10.1016/j.scriptamat.2013.01.017.
[8] A. Orozco-Caballero, D. Lunt, J.D. Robson, J. Quinta da Fonseca, Acta Mater. 133 (2017) 367–379, doi:10.1016/j.actamat.2017.05.040.
[9] J. Sun, L. Jin, J. Dong, W. Ding, A.A. Luo, Mater. Charact. 119 (2016) 195–199, doi:10.1016/j.matchar.2016.08.003.
[10] B. Xi, G. Fang, S. Xu, Mater. Charact. 135 (2018) 115–123, doi:10.1016/j.matchar.2017.11.034.
[11] M.R. Barnett, S. Jacob, B.F. Gerard, J.G. Mullins, Scr. Mater. 59 (2008) 1035–1038, doi:10.1016/j.scriptamat.2008.06.061.
[12] W.H. Hartt, R.E. Reed-Hill, Trans Met. Soc AIME. 242 (1968) 1127–1133.
[13] T. Al-Samman, G. Gottstein, Mater. Sci. Eng. A 488 (2008) 406–414, doi:10.1016/j.msea.2007.11.056.
[14] D.A. Basha, H. Somekawa, A. Singh, Scr. Mater. 142 (2018) 50–54, doi:10.1016/j.scriptamat.2017.08.023.
[15] T. Hama, H. Takuda, Comput. Mater. Sci. 51 (2012) 156–164, doi:10.1016/j.commatsci.2011.07.026.
[16] D. Steglich, Y. Jeong, M.O. Andar, T. Kuwabara, Int. J. Solids Struct. 49 (2012) 3551–3561, doi:10.1016/j.ijsolstr.2012.06.017.
[17] D. Steglich, X. Tian, J. Bohlen, T. Kuwabara, Exp. Mech. 54 (2014) 1247–1258, doi:10.1007/s11340-014-9892-0.
[18] J. Blaber, B. Adair, A. Antoniou, Exp. Mech. 55 (2015) 1105–1122, doi:10.1007/s11340-015-0009-1.
[19] Y. Seymen, B. Güler, M. Efe, Exp. Mech. 56 (2016) 1519–1530, doi:10.1007/s11340-016-0185-7.
[20] P.A.F. Martins, N. Bay, A.E. Tekkaya, A.G. Atkins, Int. J. Mech. Sci. 83 (2014) 112–123, doi:10.1016/j.ijmecsci.2014.04.003.
[21] J. Koike, R. Ohyama, T. Kobayashi, M. Suzuki, K. Maruyama, Mater. Trans. 44 (2003) 445–451, doi:10.2320/matertrans.44.445.
[22] P.D. Wu, X.Q. Guo, H. Qiao, D.J. Lloyd, Mater. Sci. Eng. A. 625 (2015) 140–145, doi:10.1016/j.msea.2014.11.096.
[23] B.C. Suh, J.H. Kim, J.H. Hwang, M.S. Shim, N.J. Kim, Sci. Rep. 6 (2016) 1–8, doi:10.1038/srep22364.
[24] H. Somekawa, A. Singh, T. Mukai, Philos. Mag. Lett. 89 (2009) 2–10, doi:10.1080/09500830802537718.
[25] M.D. Nave, M.R. Barnett, Scr. Mater. 51 (2004) 881–885, doi:10.1016/j.scriptamat.2004.07.002.
[26] D. Ando, J. Koike, Y. Sutou, Mater. Sci. Eng. A. 600 (2014) 145–152, doi:10.1016/j.msea.2014.02.010.
[27] B. Wang, L. Deng, C. Adrien, N. Guo, Z. Xu, Q. Li, Mater. Charact. 108 (2015) 42–50, doi:10.1016/j.matchar.2015.08.014.